Scilight

Advanced Characterization

https://www.sciltp.com/journals/ac

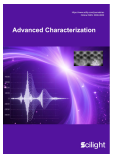

Article

Enhanced Removal of Uranium(VI) by Nitrogen-Modified Zerovalent Iron Synthesized via Mechanochemically Ball Milling

Lianjie Ma [1,2], Peng Fan [2,*], Kunming Hou [2], Zhengwu Liu [3], Meng Du [2], Chen Tian [2], Zhenye Liang [3], Bing Nan [2], Luozhen Jiang [2], Lingling Guo [2], Yulin Qin [2], Zhuofan Zhang [2], Jisong Mi [2], Yingpeng Xie [1,*] and Lina Li [2,3,*]

[1] College of Chemical Engineering, Shenyang University of Chemical Technology, Shenyang 110142, China
[2] Shanghai Synchrotron Radiation Facility, Shanghai Advanced Research Institute, Chinese Academy of Sciences, Shanghai 201204, China
[3] Shanghai Institute of Applied Physics, Chinese Academy of Sciences, Shanghai 201204, China
* Correspondence: fanp@sari.ac.cn (P.F.); ypxie@syuct.edu.cn (Y.X.); lilina@sinap.ac.cn (L.L.); Tel.: +86-21-55272920 (P.F.); +86-24-89385030 (Y.X.); +86-21-33932213 (L.L.)

How To Cite: Ma, L.; Fan, P.; Hou, K.; et al. Enhanced Removal of Uranium(VI) by Nitrogen-Modified Zerovalent Iron Synthesized via Mechanochemically Ball Milling. *Advanced Characterization* **2026**, *1*(1), 1–11.

Received: 15 January 2026
Revised: 17 March 2026
Accepted: 18 March 2026
Published: 30 March 2026

Abstract: The remediation of uranium (U(VI)) contamination in water is of critical importance due to its chemical toxicity, long-term radiotoxicity, and environmental mobility. This study employed a green and efficient mechanical ball-milling method, using melamine as a nitrogen source, to successfully synthesize a nitrogen-modified zerovalent iron material (N-ZVI^{bm}). Systematic characterization, revealed that the ball-milling process successfully constructed Fe–N_x coordination structures on the ZVI surface. This structure optimized the electronic distribution of zerovalent iron and enhanced its surface reactivity. Batch experiments demonstrated that the U(VI) removal by N-ZVI^{bm} follows pseudo-first-order kinetics, exhibiting a rate constant as high as 0.288 h^{-1}, which is 3.7 times that of unmodified ball-milled zerovalent iron (ZVI^{bm}). Mechanistic studies revealed that the Fe–N_x sites not only promoted the corrosion of ZVI, accelerating the formation of adsorptive iron(III) (oxyhydr) oxides, but also functioned as highly efficient adsorption and electron transfer sites, synergistically enhancing both the adsorption and reduction of U(VI). Post-reaction solid analysis indicated a U(IV) content of up to 68%, markedly exceeding that in the control system (29%), confirming the efficacy of nitrogen modification in enhancing U(VI) reduction and immobilization. This work not only establishes a novel green pathway for synthesizing high-performance zerovalent iron materials but also deepens the understanding of the mechanisms of Fe–N_x structures in radionuclide remediation.

Keywords: zerovalent iron; ball milling; uranium removal; X-ray absorption fine structure; wastewater remediation

1. Introduction

The Fukushima nuclear accident generated vast quantities of radioactive wastewater, with the current accumulated volume exceeding one million tonnes, posing significant threats to both the environment and human health [1]. This wastewater predominantly contains uranium (U) in the form of highly soluble and mobile UO_2^{2+} ions and their complexes [2,3]. With a half-life ranging from hundreds of thousands to 4.5 billion years, uranium is one of the primary radionuclides of concern. Its inherent chemical toxicity and radiotoxicity pose severe risks to human health [4]. Moreover, uranium serves as a vital nuclear fuel, playing a significant role in producing clean,

low-carbon energy [5,6]. Consequently, recovering uranium from nuclear wastewater is crucial for environmental protection, safeguarding human health, and advancing industrial development.

Micron-sized zerovalent iron (mZVI) and nano-zerovalent iron (nZVI) technologies exhibit strong reducing properties, straightforward operation, and environmental friendliness [7–9]. They can remove various pollutants through multiple mechanisms, including reduction, adsorption, coprecipitation, and the generation of reactive oxygen species [10–12]. Consequently, they are widely applied in the treatment of heavy metals and radionuclides in wastewater. However, nZVI has a strong tendency to agglomerate and passivate during reactions. When employed for in situ groundwater remediation, nZVI particles demonstrate severely limited mobility in porous media such as soil and aquifers [13,14]. In contrast, mZVI is considered one of the most promising materials for treating heavy metals and remediating radionuclides, owing to its low cost, environmental benignity, and easily tunable surface structure [15,16].

However, traditional ZVI suffers from drawbacks such as passivation, low electron utilization efficiency, and poor reaction selectivity, which limit its practical application [17]. Consequently, various modification techniques have been developed to enhance ZVI reactivity, primarily including reduction pretreatment [18,19], fabrication of bimetallic compounds [20], coupling with chemicals [21], and doping with heteroatoms [7,22]. The synthesis of novel modified ZVI materials mainly employs liquid-phase and mechanochemical methods [23,24]. The conventional liquid-phase synthesis requires excessive solvents, leading to potential secondary pollution, operational complexity, and limited yield. In recent years, mechanochemically ball milling has emerged as an innovative and environmentally friendly synthesis technique, experiencing rapid development [25]. Ball-milling technology can break the oxide layer on ZVI through mechanical activation, exposing fresh active surfaces and demonstrating excellent modification potential. Concurrently, doping with non-metallic elements (such as nitrogen [26,27], sulfur [11,28], or boron [17]) has been shown to modulate the electronic structure of ZVI, enhancing its surface reactivity and stability. Among various modification strategies, nitrogen modification has garnered significant attention due to its ability to form Fe–N_x coordination structures, optimize electron distribution, provide specific adsorption sites, and promote the reduction of metal ions [29,30]. However, the current synthesis of nitrogen-modified ZVI predominantly relies on wet chemical methods, which are complex and prone to introducing impurities. Mechanical ball milling, as a green and efficient solid-state synthesis technique, enables atomic-level compositing between ZVI and nitrogen sources [31,32]. Nevertheless, its application and mechanism in U(VI) removal remain insufficiently explored.

In this study, we successfully synthesized nitrogen-modified zerovalent iron (N-ZVI^{bm}) via mechanical ball milling. Its performance in U(VI) removal was systematically evaluated, and multiple characterization techniques were employed to elucidate the surface structural evolution and reaction mechanisms. This research particularly focuses on the synergistic role of Fe–N_x sites in promoting ZVI corrosion, U(VI) adsorption, and reduction, providing a theoretical foundation and technical support for the rational design and practical application of high-efficiency ZVI materials.

2. Experimental

2.1. Chemicals

All chemicals were used as received without further purification. These primarily included zerovalent iron (ZVI, micron grade, 100 mesh, AR grade, Aladdin, Shanghai, China), melamine ($C_3H_6N_6$, ≥99%, Aladdin), uranium nitrate hexahydrate ($UO_2(NO_3)_2{\cdot}6H_2O$, ≥99%, Aladdin), anhydrous ethanol (CH_3CH_2OH, AR, Sinopharm), sodium chloride (NaCl, AR, Macklin, Shanghai, China), concentrated hydrochloric acid (HCl, 37%, AR, Sinopharm, Shanghai, China), and sodium hydroxide (NaOH, AR, Sinopharm). All stock solutions and reaction mixtures were prepared and diluted using Milli-Q ultrapure water.

2.2. Synthesis of ZVI^{bm} and N-ZVI^{bm}

The nitrogen-modified zerovalent iron (N-ZVI^{bm}) used in this study was synthesized via a mechanochemically ball milling process. Specifically, 10.0 g of raw ZVI powder was thoroughly mixed with 0.1882 g of melamine, corresponding to a N/Fe molar ratio of 0.05 [30]. The nitrogen doping ratio (N/Fe = 0.05) was selected based on a comprehensive review of previous studies on heteroatom modified zerovalent iron [7,33]. This specific molar ratio has been demonstrated to achieve an optimal balance between surface reactivity and structural integrity. A lower nitrogen content (N/Fe < 0.02) often results in insufficient active sites (Fe–N_x) for pollutant capture and electron transfer, while an excessively high dosage (N/Fe > 0.1) can lead to over-passivation of the ZVI surface or the formation of thick iron (oxyhydr) oxide layers that hinder electron transport from the Fe^0 core. The mixture was placed into a 100 mL stainless steel ball-milling jar containing 15 large stainless steel balls

(10 mm diameter) and 80 small stainless steel balls (6 mm diameter). Subsequently, 1.0 mL of anhydrous ethanol was added as a process control agent. The sealed jar was then fixed in a planetary ball mill (QM-3SP2, Nanjing Boyuntong Instrument) and ground at 500 rpm for 8 h at room temperature to obtain N-ZVI^{bm}. For comparison, unmodified ZVI (ZVI^{bm}) was prepared under identical ball-milling conditions without the addition of melamine. The resulting solid products were collected, freeze-dried for 24 h, and stored in an N_2-filled glovebox for subsequent characterization and experiments.

2.3. Batch Experiments

Batch experiments were conducted to investigate the kinetics of U(VI) removal. Each experiment was performed in a 500 mL wide-mouth flask as the reaction vessel. The reaction solution was prepared by diluting a predetermined amount of uranyl nitrate hexahydrate and background electrolyte (1.0 mM NaCl) to 500 mL with ultrapure water, yielding an initial U(VI) concentration of 50 mg/L. The initial pH of the solution was adjusted to 6.0 using diluted HCl and NaOH solutions. The reaction mixture was mechanically agitated at 400 rpm and 25 °C using an overhead stirrer with a helical impeller (D2004W, Shanghai Sile Instrument Co. Ltd., Shanghai, China). The dosage of all ZVI materials was maintained at 0.5 g/L. At predetermined time intervals, 5 mL aliquots were withdrawn using a syringe, immediately filtered through a 0.22 μm polyethersulfone membrane filter, transferred into centrifuge tubes, and acidified with 40 μL of concentrated nitric acid for preservation. The acidified samples were then sealed and stored at 4 °C prior to analysis. The kinetic experimental data were obtained from three replicate experiments and averaged.

2.4. Analytical Methods

The materials (ZVI^{bm} and N-ZVI^{bm}) before and after the reaction were characterized using the following techniques. The surface morphology and local elemental composition were examined using a scanning electron microscope (SEM, ZEISS GeminiSEM 300) equipped with an energy dispersive X-ray spectroscopy (EDS) system. The crystalline phases were identified by X-ray diffraction (XRD) on a diffractometer operated at 40 kV and 40 mA with Cu Kα radiation (λ = 1.5418 Å). XRD patterns were recorded in the 2θ range of 10° to 90° with a step size of 0.02° and a counting time of 2 s per step. Raman spectra were recorded on a Renishaw inVia Reflex spectrometer using a 532 nm excitation laser to detect the formation of Fe–N bonds on the melamine-modified ZVI surface. The primary surface elements, their chemical states, and concentrations were determined by X-ray photoelectron spectroscopy (XPS). All binding energies were calibrated relative to the C 1s peak at 284.8 eV. The total uranium concentration in the solution samples was quantified using inductively coupled plasma optical emission spectrometry (ICP-OES, Agilent, Santa Clara, CA, USA).

The valence state of uranium in the solid reaction products was characterized by X-ray absorption fine structure (XAFS) spectroscopy. Uranium *L3*-edge XAFS measurements were conducted at the BL14W beamline of the Shanghai Synchrotron Radiation Facility (SSRF, Shanghai, China). A Si(311) double-crystal monochromator was used to scan the U *L3*-edge. X-ray absorption near edge structure (XANES) spectra were collected in fluorescence mode. The line shape and peak positions of the XANES spectra showed negligible variation between two consecutive scans for a given sample. The oxidation state of uranium was determined by linear combination fitting (LCF) using standard reference compounds, including UO_2 (U(IV)) and $UO_2(NO_3)_2$ (U(VI)), provided by SSRF. The XAFS spectra of these standard samples were recorded in transmission mode and processed using the Athena software.

Iron *K*-edge XAFS measurements were performed at the 16U beamline of the SSRF. The extended X-ray absorption fine structure (EXAFS) spectra at the Fe *K*-edge were collected in transmission mode. The types of iron oxides in the samples were quantitatively analyzed by LCF using reference standards, including metallic Fe (Fe^0), hematite (α-Fe_2O_3), maghemite (γ-Fe_2O_3), goethite (α-FeOOH), lepidocrocite (γ-FeOOH), and magnetite (Fe_3O_4).

3. Results and Discussion

3.1. Structural and Chemical Characterization of Materials

Figure 1 presents the SEM images and EDS elemental mapping of ZVI before and after ball milling. SEM revealed that the pristine ZVI particles were spherical (Figure 1a), whereas the ZVI^{bm} assumed a smooth, plate-like morphology (Figure 1b). After modification with melamine (N/Fe = 0.05), the surface of N-ZVI^{bm} became rough and was covered with a layer of aggregated particles (Figure 1c). EDS mapping confirmed the uniform distribution of nitrogen on the ZVI surface after ball milling (Figure 1d–h). The EDS spectrum of N-ZVI^{bm} (Figure 1d) indicated the presence of nitrogen, carbon, oxygen, and iron, confirming the successful incorporation of N and C atoms from

melamine. The overlapping signals of Fe, N, and C suggest their proximity at the atomic level, consistent with the formation of an Fe–N_x (C) coordination phase [30]. The measured N/Fe atomic ratio by EDS was 0.043 (average of three random spots), slightly lower than the nominal value of 0.05, indicating minor nitrogen loss during ball milling, likely due to mechanochemical volatilization. Batch-to-batch reproducibility was confirmed by three independent syntheses, yielding N/Fe ratios of 0.043 ± 0.001, demonstrating good consistency. The original SEM images can be found in Supplementary Information Figures S1–S8.

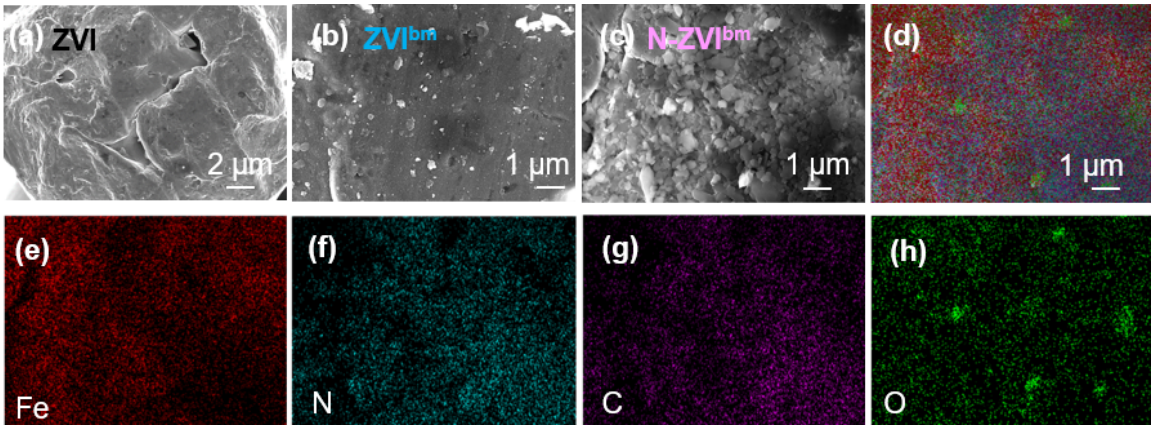

Figure 1. SEM images of ZVI (**a**); ZVI^{bm} (**b**) and N-ZVI^{bm} (**c**); EDS mapping images of Fe, N, C and O elements for N-ZVI^{bm} (**d**–**h**).

The XRD patterns of ZVI^{bm} and N-ZVI^{bm} (Figure 2a) show distinct peaks for Fe^0 at 44.7°, 65.1°, and 82.2°, corresponding to the (110), (200), and (211) planes of cubic α-Fe (PDF#98-000-0259), respectively [24]. No additional diffraction peaks corresponding to Fe–N_x (C) species were observed, suggesting that N and C were incorporated into the iron matrix in a disordered or low-crystallinity form, consistent with previous reports [34]. This indicates that the melamine modification did not alter the bulk crystal structure of ZVI. The Raman spectra (Figure 2b) of N-ZVI^{bm} exhibited distinct peak shifts compared to ZVI^{bm}. The appearance of peaks at 218 cm^{-1}, 279 cm^{-1}, and 397 cm^{-1}, assigned to Fe–N and Fe–C–N bonds [30,34], confirms the successful formation of these bonds on the ZVI surface after melamine modification [35,36].

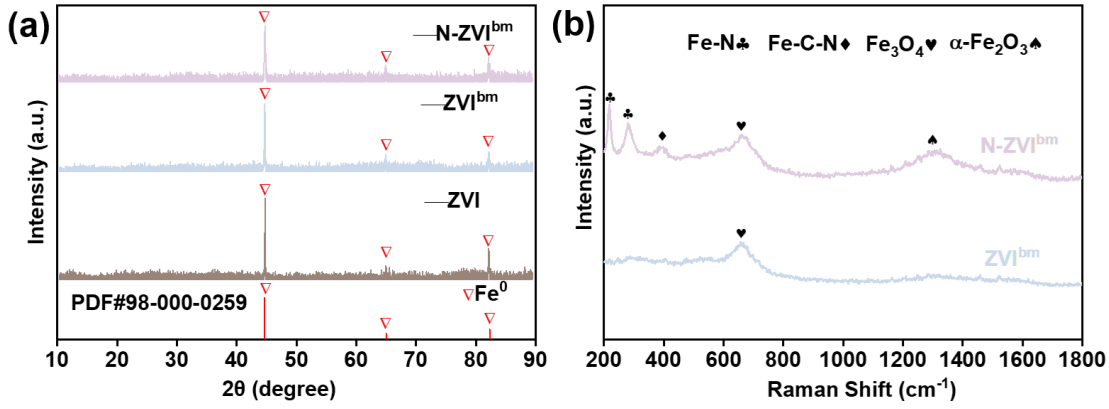

Figure 2. (**a**) The XRD patterns of ZVI, ZVI^{bm} and N-ZVI^{bm}; (**b**) Raman spectra of ZVI^{bm} and N-ZVI^{bm}.

XPS analysis further corroborated the formation of Fe–N_x bonds. The Fe 2p spectra of ZVI^{bm} and N-ZVI^{bm} before and after reaction are shown in Figure S11a–d. The Fe $2p_{3/2}$ peaks for Fe(III), Fe(II), and Fe(0) were located at approximately 712.87 eV, 710.67 eV, and 706.48 eV, respectively, while the corresponding Fe $2p_{1/2}$ peaks were observed at 726.25 eV, 724.04 eV, and 720.28 eV. After ball milling with the nitrogen source, the Fe(III) $2p_{3/2}$ and Fe(0) $2p_{1/2}$ peaks in N-ZVI^{bm} shifted to lower binding energies, indicating an electronic redistribution of iron [26]. The distribution of iron oxidation states is depicted in Figure 3a. Furthermore, comparison of the Fe *K*-edge XANES curves (Figure 3b) reveals a shift towards higher energies in the N-ZVI^{bm} curve relative to ZVI^{bm}, indicating an outward electron transfer from zerovalent iron following nitrogen modification [37,38]. The experimental results show that after ball milling with melamine, N-ZVI^{bm} exhibited slightly reduced Fe(0) and Fe(II) contents compared to ZVI^{bm}. This may result from mechanochemical reactions between Fe(0)/Fe(II) and

the nitrogen source during milling, leading to the formation of Fe–N_x complexes. This observation aligns with reports on sulfur-modified ZVI, where Fe^0 reacts with S^0 to form FeS, decreasing the Fe^0 content [39].

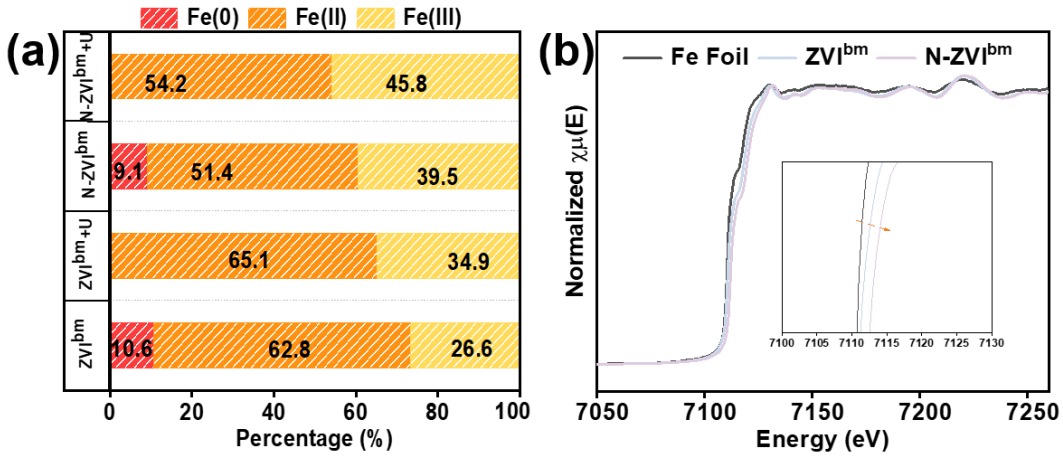

Figure 3. (**a**) Molar fraction of Fe(0), Fe(II), and Fe(III) derived from fitting of XPS Fe 2p spectra; (**b**) Normalized Fe *K*-edge XANES spectra of the ZVI^{bm} and N-ZVI^{bm}.

Figure S9 shows the N 1s XPS spectrum of N-ZVI^{bm}. The deconvoluted peaks at 398.6 eV, 399.5 eV, and 400.6 eV are assigned to pyridinic N, pyrrolic N, and graphitic N, accounting for 65%, 32%, and 3% of the total nitrogen content, respectively. In contrast, the N1s spectrum of ZVI^{bm} exhibits no distinct peaks, confirming the absence of nitrogen. Both pyridinic N and pyrrolic N provide lone pair electrons, which can serve as metal coordination sites for activating reactants. Graphitic N acts as an electron transfer mediator in N-C-Fe-driven redox reactions, facilitating electron donation from the zerovalent iron core [31,40]. The abundant pyridinic N content in N-ZVI^{bm} indicates the formation of Fe–N structures. Furthermore, the covalent bonding between adjacent N atoms and Fe partially depletes the electron density of Fe, forming M–N configurations that provide sufficient coordination sites for the positively charged Fe centers [41].

The combined Raman and XPS analyses confirm that Fe–N_x structures form on the ZVI surface after melamine modification. Fe–N_x materials typically possess a large specific surface area, with nitrogen atoms acting as favorable coordination sites capable of forming stable complexes with heavy metal ions.

3.2. Effect of Nitrogen Modification on U(VI) Removal Performance by ZVI

The U(VI) removal performance of N-ZVI^{bm} was compared with that of ZVI^{bm}. The kinetics of U(VI) removal by both materials followed a pseudo-first-order kinetic model. The removal rate constant of N-ZVI^{bm} (0.288 h^{-1}) was 3.7 times that of ZVI^{bm} (0.077 h^{-1}) (Figure 4), demonstrating that nitrogen modification significantly enhances the reactivity of ZVI towards U(VI).

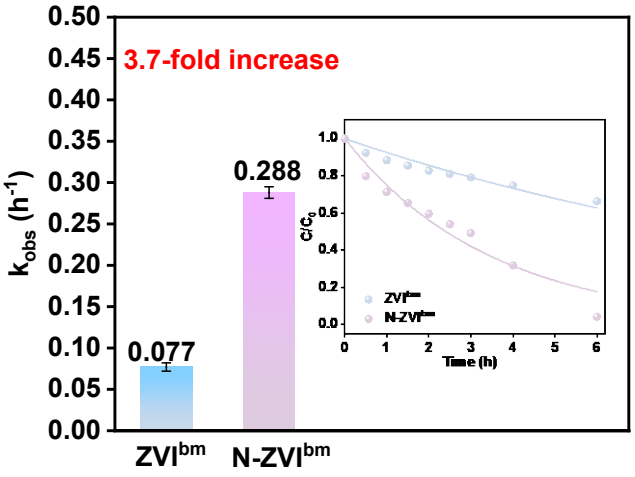

Figure 4. ZVI^{bm} and N-ZVI^{bm} rate constants for U(VI) removal and pseudo-first-order kinetic fitting. $[U(VI)]_0$ = 50mg/L, $[ZVI^{bm}]_0$ = $[N\text{-}ZVI^{bm}]_0$ = 0.5 g/L, initial pH 6.0.

3.3. Mechanism for the Removal of Uranium (VI)

3.3.1. ZVI Corrosion and Subsequent U(VI) Adsorption by Corrosion Products

To better understand the U(VI) removal mechanism by ZVI^{bm} and N-ZVI^{bm}, the corrosion behavior of ZVI in both materials before and after the reaction was analyzed and compared. The Fe 2p XPS spectra of ZVI^{bm} and N-ZVI^{bm} before and after the reaction were first examined (Figure S11a–d). Before the reaction, Fe^0 was present as a minor component on the surfaces of both materials, indicating partial surface oxidation of ZVI by atmospheric oxygen, forming an iron oxide layer. After the reaction, the Fe^0 peak completely disappeared from the material surfaces, confirming its corrosion to Fe(II) and Fe(III). The relative proportions of Fe species are depicted in Figure 3a.

To further elucidate the effect of nitridation on ZVI corrosion, Fe *K*-edge EXAFS spectra were collected from the ZVI^{bm} and N-ZVI^{bm} systems before and after U(VI) removal (Figure 5a). LCF analysis of the Fe *K*-edge EXAFS spectra quantified the proportions of different iron oxides in the solid phases before and after the reaction for both systems (Figure 5b and Table S1). Before the reaction, Fe^0 was the predominant component (the iron oxides on the ZVI surface accounted for a negligible proportion). For the N-ZVI^{bm} system, minor amounts of Fe(II) and Fe(III) were already present, indicating reaction between ZVI and the nitrogen source during ball milling, further corroborating the formation of Fe–N_x.

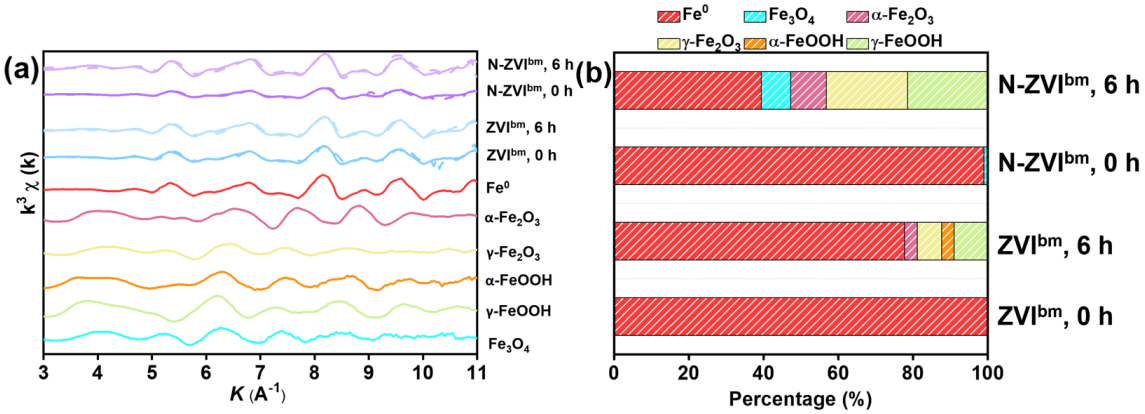

Figure 5. (**a**) Fe k^3-weighted EXAFS spectra of solid-state Fe samples before and after ZVI^{bm} and N-ZVI^{bm} system reactions; (**b**) The proportion of various Fe(III) oxides in solid precipitate samples obtained after different reaction times, derived from LCF fitting of Fe k^3-weighted EXAFS spectra for the ZVI^{bm} and N-ZVI^{bm} systems undergoing U(VI) removal.

The corrosion of Fe^0 generally proceeds via reactions such as:

$$3Fe^0 + 4H_2O \rightarrow Fe_3O_4 + 4H_2 \quad (1)$$

$$4Fe^0 + 3O_2 + 2H_2O \rightarrow 4\alpha - FeOOH \quad (2)$$

$$4Fe^0 + 3O_2 + 2H_2O \rightarrow 4\gamma - FeOOH \quad (3)$$

$$2\gamma - FeOOH \rightarrow \gamma - Fe_2O_3 + H_2O \quad (4)$$

$$2\alpha - FeOOH \rightarrow \alpha - Fe_2O_3 + H_2O \quad (5)$$

Analysis of the proportions of various iron oxides after the reaction revealed that the remaining Fe^0 content in the N-ZVI^{bm} system was significantly lower than in the ZVI^{bm} system, with Fe_3O_4, γ-Fe_2O_3, and γ-FeOOH being the primary corrosion products. These corrosion products are key active components for removing heavy metal ions from water [33,42]. The hydroxyl groups (≡Fe–OH) on the surface of iron oxides can act as amphoteric groups in aqueous solution, participating in surface complexation (ion exchange) with heavy metal ions [42]. For UO_2^{2+}, inner-sphere surface complexation is the primary mechanism, where UO_2^{2+} directly displaces H^+ from the ≡Fe–OH groups or forms strong chemical bonds with oxygen atoms, generating stable inner-sphere surface complexes (e.g., ≡FeO–UO_2^+). This interaction is highly specific and strong, leading to the robust immobilization of U(VI) on the surface. Furthermore, electrostatic interactions play a significant role [2]. Under near-neutral or weakly acidic conditions (pH 6.0 in this study), some iron oxide surfaces may be positively charged or neutral, favoring the adsorption of anionic uranyl hydroxyl complexes (e.g., $UO_2(OH)_3^-$) through electrostatic attraction.

Although the initial pH was set to 6.0, ZVI corrosion typically consumes H^+, leading to a gradual increase in pH during the reaction [43]. This pH drift may influence uranium speciation-at near-neutral to slightly alkaline conditions, U(VI) tends to form hydrolyzed species such as $UO_2(OH)_3^-$, which could alter adsorption affinity toward iron oxides [6]. Moreover, the surface charge of corrosion products is pH-dependent, potentially affecting electrostatic interactions [42]. Nevertheless, the consistent comparison between ZVI^{bm} and N-ZVI^{bm} under identical initial pH conditions validates the enhanced reactivity conferred by nitrogen modification.

The Fe–N_x sites also play a synergistic role. As previously mentioned, the Fe–N_x sites themselves serve as highly efficient adsorption centers. Nitrogen atoms (e.g., pyridinic N) on these sites can undergo specific coordination with UO_2^{2+}, further enhancing the initial adsorptive enrichment.

3.3.2. Synergism between Adsorptive and Reductive Pathways

For both micro- and nano-sized ZVI, adsorption and reduction are crucial mechanisms for removing radionuclides (e.g., UO_2^{2+} [2], ReO_4^- [44], TcO_4^- [45]) and heavy metal ions (e.g., Ni^{2+} [37], Cr^{6+} [11], Pb^{2+} [12]).

To investigate the U(VI) removal mechanism by ZVI, the U 4f XPS spectra of the solids after a 6-h reaction with N-ZVI^{bm} and ZVI^{bm} were examined (Figure S12). Distinct peaks for both U(VI) and U(IV) are clearly observable in the U 4f XPS spectra of both N-ZVI^{bm} and ZVI^{bm}, indicating that both adsorption and reduction mechanisms contribute concurrently to U(VI) removal. Different types of nitrogen elements play distinct roles in modifying zero-valent iron surfaces. Pyridinic N possesses a lone pair of electrons localized in the plane of the carbon ring, making it a strong Lewis base that readily coordinates with Lewis acidic UO_2^{2+} ions [46]. In contrast, pyrrolic N donates its lone pair to the aromatic π-system, reducing its availability for direct metal binding. Graphitic N, while not directly coordinating, enhances the overall electrical conductivity of the material and facilitates electron transfer from the Fe^0 core to the surface-bound U(VI) [47]. Therefore, the high proportion of pyridinic N (65%) in N-ZVI^{bm} is particularly advantageous: it not only provides abundant adsorption sites for U(VI) via coordination [48], but also, upon coordination, activates the U-O bonds and lowers the energy barrier for subsequent reduction. The Fe–N_x sites thus serve a dual function-adsorption centers and electron bridges-with pyridinic N playing the key role in both steps.

Fe^0 is a strong electron donor ($E^0(Fe^{2+}/Fe^0) = -0.44$ V) [7]. The UO_2^{2+} ions, immobilized by adsorption onto the surface iron oxides or Fe–N_x sites, experience a shortened spatial distance to the Fe^0 core, enabling them to accept electrons directly from Fe^0, leading to the reaction (Equation (6)). This process generates UO_2, a sparingly soluble U(IV) solid with low crystallinity that precipitates stably on or within the material, thereby immobilizing the uranium. Furthermore, Fe(II) species generated during ZVI corrosion, including aqueous Fe^{2+} and structural Fe(II) within solids, serve as another important reductant [24]. The Fe(II)/Fe(III) redox cycle is crucial for U(VI) reduction (Equation (7)). On one hand, Fe(II) adsorbed onto iron oxide surfaces can directly transfer electrons to co-adsorbed UO_2^{2+}. On the other hand, some Fe(II) can be stabilized by surface ≡Fe(III)–OH sites, forming highly reactive surface complexes that reduce U(VI) more effectively.

$$Fe^0 + UO_2^{2+} \rightarrow Fe^{2+} + UO_2 \quad (6)$$

$$2Fe^{2+} + UO_2^{2+} \rightarrow 2Fe^{3+} + UO_2 \quad (7)$$

The Fe–N_x structures introduced by nitrogen modification play the role of an “electron bridge” in the reduction process. The strong electronic coupling between the Fe–N_x sites and the ZVI core significantly facilitates electron migration from the Fe^0 core to the material surface [30,49]. The Fe–N_x sites first undergo specific coordination with UO_2^{2+}, activating the UO_2^{2+} molecule and weakening its O=U=O bonds, thereby lowering the energy barrier for the subsequent reduction reaction. Acting as efficient electron shuttles, the Fe–N_x sites preferentially and rapidly transfer electrons-conducted from the Fe^0 core-to the coordinated UO_2^{2+}, greatly accelerating the conversion of U(VI) to U(IV). This is evidenced by the markedly larger U(IV) peak area in the N-ZVI^{bm} system compared to ZVI^{bm}, reaching 68%, whereas the U(IV) peak area in the ZVI^{bm} system was only 29%. This indicates that most of the U(VI) adsorbed onto N-ZVI^{bm} was reduced to U(IV), demonstrating that nitrogenation of ZVI promotes the reduction process of U(VI).

To further elucidate the U(VI) removal mechanism by ZVI, U *L3*-edge XANES spectra were collected from the solid products after the U(VI) removal reaction in both ZVI^{bm} and N-ZVI^{bm} systems. LCF analysis of the U *L3*-edge XANES spectra (Figure 6a,b) identified peaks corresponding to UO_2^{2+} and UO_2, further confirming that the removal mechanisms in both systems involve both adsorption and reduction. The figures show that the proportion of U_3O_8 is comparable in different systems and constitutes the primary component. The proportion of UO_2 in the N-ZVI^{bm} system (28.1%) is significantly higher than that in the ZVI^{bm} system (7.3%), consistent with the XPS results. Notably, the surface U(IV) fractions derived from XPS analysis (68% for N-ZVI^{bm} and 29% for

ZVI^{bm}) are substantially higher than the bulk UO_2 proportions obtained from U *L*3-edge XANES linear combination fitting. This discrepancy can be attributed to the different probing depths of the two techniques. As a surface-sensitive method with an information depth of less than 10 nm, XPS captures the uranium speciation primarily at the outermost layer of the particles, revealing a preferential enrichment of U(IV) products on the ZVI surface. In contrast, XANES provides an averaged bulk signal across the entire particle, and the relatively lower U(IV) content reflects signal dilution from the interior regions where unreacted or only adsorbed U(VI) species may dominate. Despite the numerical differences, the trends obtained from both techniques are highly consistent N-ZVI^{bm} exhibits a markedly higher U(IV) proportion than ZVI^{bm} in both surface and bulk analyses. This agreement robustly demonstrates that nitrogen modification not only promotes U(VI) reduction at the surface layer but also significantly enhances the overall reduction capability of the material. These findings strongly support the central role of Fe–N_x structures in facilitating the synergistic adsorption-reduction mechanism. This again demonstrates the promoting effect of nitrogen-modified ZVI on the reduction of U(VI).

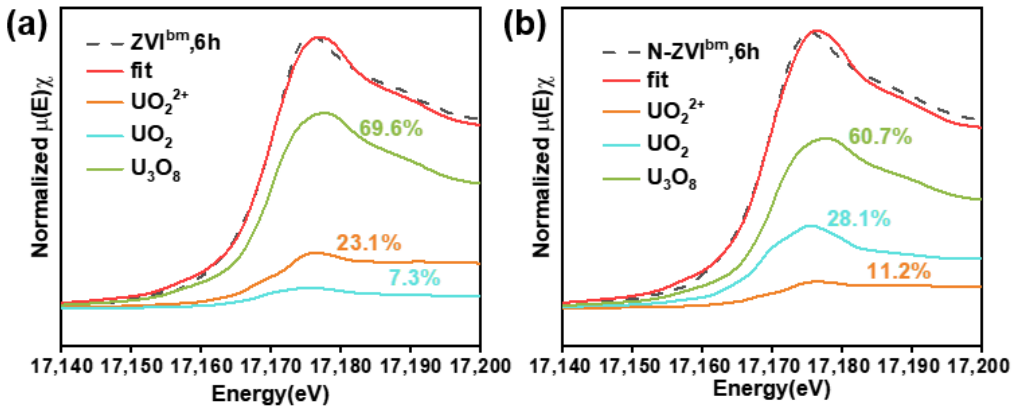

Figure 6. U *L3*-edge X-ray absorption near edge structure (XANES) spectra and the linear combination fits (LCF) results of the ZVI^{bm} (**a**) and N-ZVI^{bm} (**b**) systems.

4. Conclusions

In summary, we have demonstrated that mechanical ball-milling modification using melamine as a nitrogen source significantly enhances the U(VI) removal performance of ZVI. The introduction of nitrogen forms an Fe–N_x coordination structure on the ZVI surface, which optimizes its electronic structure and enhances surface reactivity. This Fe–N_x structure accelerates ZVI corrosion, promoting the generation of Fe^{3+}/Fe^{2+} (oxyhydr) oxides that provide additional adsorption sites. Furthermore, the proportion of U(IV) in the reaction products was markedly higher for N-ZVI^{bm} than for ZVI^{bm}, confirming that nitrogen modification effectively enhances the reduction and immobilization of U(VI). The Fe–N_x sites function not only as coordination centers to enhance U(VI) adsorption but also as electron bridges facilitating interfacial electron transfer, achieving a synergistic adsorption-reduction effect. This mechanochemical nitrogen modification enables N-ZVI^{bm} to achieve a U(VI) removal rate constant of 0.288 h^{-1}, which is 3.7 times that of ZVI^{bm}, demonstrating accelerated reaction kinetics and higher removal capacity. This study confirms the applicability of N-ZVI^{bm} for remediating U(VI) contaminated wastewater. It provides a green and efficient synthetic pathway for nitrogen-modified ZVI while deepening the understanding of the mechanism of Fe–N_x structures in heavy metal remediation.

Supplementary Materials

The additional data and information can be downloaded at: https://media.sciltp.com/articles/others/260330144348079 3/AC-26010082-SM-FC-done.pdf. Figure S1: SEM images of ZVI. Figure S2: SEM images of ZVI^{bm}. Figure S3: SEM images of N-ZVI^{bm}. Figure S4: EDS mapping images of all elements for N-ZVI^{bm}. Figure S5: EDS mapping images of Fe element for N-ZVI^{bm}. Figure S6: EDS mapping images of N element for N-ZVI^{bm}. Figure S7: EDS mapping images of C element for N-ZVI^{bm}. Figure S8: EDS mapping images of O element for N-ZVI^{bm}. Figure S9: XPS spectra of N 1s for the N−ZVI^{bm}. Figure S10: XPS spectra of C 1s for the N−ZVI^{bm}. Figure S11: XPS spectra of Fe 2p before and after ZVI^{bm} and N-ZVI^{bm} reactions (a–d). Figure S12: XPS spectra of the ZVI^{bm} (a) and N-ZVI^{bm} (b) systems U4f. Table S1: The proportion of various Fe(III) oxides in solid precipitate samples obtained after different reaction times.

Author Contributions

L.M.: writing—review & editing, writing—original draft, validation, resources, methodology, investigation, formal analysis, data curation; P.F.: writing—review & editing, writing—original draft, resources, project administration, methodology, data curation; K.H.: methodology, formal analysis; Z.L. (Zhengwu Liu): formal analysis, data curation; C.T.: formal analysis; M.D., Z.L. (Zhenye Liang), B.N., L.J., L.G., Y.Q., Z.Z. and J.M.: methodology; Y.X.: writing—review & editing, writing—original draft, methodology, data curation; L.L.: writing—review & editing, writing—original draft, validation, resources, methodology, data curation. All authors have read and agreed to the published version of the manuscript.

Funding

This work was funded by National Natural Science Foundation of China (Grants No. 22332003, 22306066), Shanghai Municipal Science and Technology Commission (Grants No. 23JC1403300). This work was also supported by Photon Science Research Center for Carbon Dioxide, 2025 Research Equipment Project of the Special Fund for Improving Research Conditions in Central-Level Scientific Institutions, Chinese Academy of Sciences and Shanghai Municipal Science and Technology Major Project.

Institutional Review Board Statement

Not applicable.

Informed Consent Statement

Not applicable.

Data Availability Statement

Data will be made available on request.

Acknowledgments

We thank the Shanghai Synchrotron Radiation Facility of Experiment Assist System (https://cstr.cn/31124.02.SSRF.LAB) for the assistance on the SEM tests. We thank the beamline BL16U1 and BL14W at SSRF for providing the beam time. We appreciate the assistance of TILON Group Technology Limited (Division of China) in characterization of catalysts.

Conflicts of Interest

The authors declare no conflict of interest.

Use of AI and AI-Assisted Technologies

No AI tools were utilized for this paper.

References

1. An, R.; Li, X.; Xie, Y. Post-Fukushima Innovation: Establishing a Regional Marine Environmental Cooperation Mechanism in Northeast Asia with Global Implications. *Front. Mar. Sci.* **2025**, *12*, 1578912.
2. Deng, S.; Yang, Y.; Han, X.; et al. Unlocking the Potential of Surface Modification with Phosphate on Ball Milled Zero-Valent Iron Reactivity: Implications for Radioactive Metal Ions Removal. *Water Res.* **2024**, *260*, 121912.
3. Lin, T.; Chen, T.; Jiao, C.; et al. Ion Pair Sites for Efficient Electrochemical Extraction of Uranium in Real Nuclear Wastewater. *Nat. Commun.* **2024**, *15*, 4149.
4. Nayak, T.; Mukherjee, S.; Kini, A.R.; et al. Cellulose-Derived Nanomaterials for Affordable and Rapid Remediation of Uranium in Water. *ACS Sustain. Chem. Eng.* **2025**, *13*, 1838–1850.
5. Liu, X.; Xie, Y.; Hao, M.; et al. Secondary Metal Ion-Induced Electrochemical Reduction of U(VI) to U(IV) Solids. *Nat. Commun.* **2024**, *15*, 7736.
6. Zhou, L.; Li, Y.; Shao, Y.; et al. Interface Coupling Induced Built-In Electric Fields Accelerate Electro-Assisted Uranium Extraction over Co_3O_4@FeO_x Nanosheet Arrays. *Appl. Catal. B* **2024**, *353*, 124052.
7. Fan, P.; Li, L.; Sun, Y.; et al. Selenate Removal by Fe^0 Coupled with Ferrous Iron, Hydrogen Peroxide, Sulfidation, and Weak Magnetic Field: A Comparative Study. *Water Res.* **2019**, *159*, 375–384.

8. Chen, J.; Feng, Y.; Liu, Y.; et al. MoS_2 Modification to Enhance the Removal of Various Chlorinated Hydrocarbons by Zerovalent Iron. *Environ. Sci. Technol.* **2025**, *59*, 11330–11340.
9. Korpayev, S.; Kavaklı, C.; Kavaklı, P.A. Nanoscale Zerovalent Iron Immobilized on Functionalized Nonwoven Cotton Fabric for As(V) Adsorption. *Water Air Soil Pollut.* **2021**, *232*, 131.
10. Fan, P.; Guan, X.; Wei, G.; et al. Simply Closing the Reactor Improves the Electron Efficiency of Zerovalent Iron toward Various Metal(loid)s Removal. *Water Environ. Res.* **2021**, *93*, 1829–1836.
11. Li, J.; Zhang, X.; Liu, M.; et al. Enhanced Reactivity and Electron Selectivity of Sulfidated Zerovalent Iron toward Chromate under Aerobic Conditions. *Environ. Sci. Technol.* **2018**, *52*, 2988–2997.
12. Zhang, H.; Liu, X.; Zhou, B.; et al. Phosphorylated Zerovalent Iron Boosts Active Hydrogen Species Generation from Water Dissociation for Superior Hg(II) Reduction. *Water Res.* **2025**, *283*, 123787.
13. Yin, Y.; Shen, C.; Liu, Y.; et al. Use of Hollow Mesoporous Silica Spheres as Vehicles for Delivery of Nanoscale Zerovalent Iron in Porous Media. *Microporous Mesoporous Mater.* **2023**, *362*, 112755.
14. Vasarevičius, S.; Danila, V.; Januševičius, T. Immobilisation of Cadmium, Copper, Lead, and Nickel in Soil Using Nano Zerovalent Iron Particles: Ageing Effect on Heavy Metal Retention. *Water Air Soil Pollut.* **2020**, *231*, 496.
15. He, C.-S.; Ding, R.-R.; Zhou, G.-N.; et al. Coexistence of Humic Acid Enhances the Reductive Removal of Diatrizoate via Depassivating Zero-Valent Iron under Aerobic Conditions. *J. Mater. Chem. A* **2020**, *8*, 14634–14643.
16. Gao, P.; Fan, X.; Sun, D.; et al. Recent Advances in Ball-Milled Materials and Their Applications for Adsorptive Removal of Aqueous Pollutants. *Water* **2024**, *16*, 1639.
17. Wei, K.; Li, H.; Gu, H.; et al. Strained Zero-Valent Iron for Highly Efficient Heavy Metal Removal. *Adv. Funct. Mater.* **2022**, *32*, 2200498.
18. Matheson, L.J.; Tratnyek, P.G. Reductive Dehalogenation of Chlorinated Methanes by Iron Metal. *Environ. Sci. Technol.* **1994**, *28*, 2045–2053.
19. Bharti; Khurana, I.; Shaw, A.K.; et al. Removal of Trinitrotoluene with Nano Zerovalent Iron Impregnated Graphene Oxide. *Water Air Soil Pollut.* **2017**, *229*, 17.
20. O'Carroll, D.; Sleep, B.; Krol, M.; et al. Nanoscale Zero Valent Iron and Bimetallic Particles for Contaminated Site Remediation. *Adv. Water Resour.* **2013**, *51*, 104–122.
21. Li, M.; Mu, Y.; Shang, H.; et al. Phosphate Modification Enables High Efficiency and Electron Selectivity of nZVI toward Cr(VI) Removal. *Appl. Catal. B* **2020**, *263*, 118364.
22. Zhu, X.; Han, B.; Feng, Q. Common Anions Affected Removal of Carbon Tetrachloride in Groundwater Using Granular Sponge Zerovalent Iron. *Water Air Soil Pollut.* **2020**, *231*, 138.
23. Li, J.; Zhang, X.; Sun, Y.; et al. Advances in Sulfidation of Zerovalent Iron for Water Decontamination. *Environ. Sci. Technol.* **2017**, *51*, 13533–13544.
24. Fan, P.; Sun, Y.; Lei, H.; et al. Mechanochemically Ball-Milled Zerovalent Iron and Ferrous Composite for Effective Removal of Various Metal(loid)s from Water. *Chem. Eng. J.* **2023**, *452*, 139380.
25. Jones, A.C.; Leitch, J.A.; Raby-Buck, S.E.; et al. Mechanochemical Techniques for the Activation and Use of Zero-Valent Metals in Synthesis. *Nat. Synth.* **2022**, *1*, 763–775.
26. Shi, Y.; Wang, D.; Gao, F.; et al. Mechanochemical Nitridation of Micron Zero-Valent Iron for Enhanced Dechlorination of Trichloroethylene: Mechanistic Insights into Nitrogen Sources and Ball Milling Conditions. *Sep. Purif. Technol.* **2024**, *337*, 126381.
27. Liu, G.-h.; Zhu, S.-N.; Ye, Z. Reduction in the Acute Toxicity of Explosive Wastewater Containing Toxic Nitroaromatic Compounds by a Nanoscale Zerovalent Iron Pretreatment Process. *Water Air Soil Pollut.* **2012**, *223*, 5049–5055.
28. He, M.-F.; Li, W.-Q.; Xie, Z.-H.; et al. Peracetic Acid Activation by Mechanochemically Sulfidated Zero Valent Iron for Micropollutants Degradation: Enhancement Mechanism and Strategy for Extending Applicability. *Water Res.* **2022**, *222*, 118887.
29. Tan, X.; Li, H.; Zhang, W.; et al. Square-Pyramidal Fe–N_4 with Defect-Modulated O-Coordination: Two-Tier Electronic Structure Fine-Tuning for Enhanced Oxygen Reduction. *Chem Catal.* **2022**, *2*, 816–835.
30. Gong, L.; Qiu, X.; Tratnyek, P.G.; et al. FeN_X(C)-Coated Microscale Zero-Valent Iron for Fast and Stable Trichloroethylene Dechlorination in Both Acidic and Basic pH Conditions. *Environ. Sci. Technol.* **2021**, *55*, 5393–5402.
31. Meng, F.; Xu, J.; Dai, H.; et al. Even Incorporation of Nitrogen into Fe^0 Nanoparticles as Crystalline Fe4N for Efficient and Selective Trichloroethylene Degradation. *Environ. Sci. Technol.* **2022**, *56*, 4489–4497.
32. Zhang, L.; Sun, Y.; Ge, R.; et al. Mechanical Insight into Direct Singlet Oxygen Generation Pathway: Pivotal Role of FeN_4 Sites and Selective Organic Contaminants Removal. *Appl. Catal. B* **2023**, *339*, 123130.
33. Fan, P.; Sun, Y.; Zhou, B.; et al. Coupled Effect of Sulfidation and Ferrous Dosing on Selenate Removal by Zerovalent Iron Under Aerobic Conditions. *Environ. Sci. Technol.* **2019**, *53*, 14577–14585.
34. Gong, L.; Qiu, X.; Cheng, D.; et al. Coincorporation of N and S into Zero-Valent Iron to Enhance TCE Dechlorination: Kinetics, Electron Efficiency, and Dechlorination Capacity. *Environ. Sci. Technol.* **2021**, *55*, 16088–16098.

35. Li, X.; Zhang, X.; Zhang, P.; et al. Incorporation of N-Doped Biochar into Zero-Valent Iron for Efficient Reductive Degradation of Neonicotinoids: Mechanism and Performance. *Biochar* **2023**, *5*, 78.
36. Smit, E.; Manoun, B.; Waal, D. Low-Wavenumber Raman Spectra of the Spin-Transition Complexes $[Fe(NH_2\ trz)_3](ClO_4)_2$ and $[Fe(Htrz)_3](ClO_4)_2$. *J. Raman Spectrosc.* **2001**, *32*, 339–344.
37. Zu, J.; Zhang, N.; Liu, X.; et al. Mechanochemical Thioglycolate Modification of Microscale Zero-Valent Iron for Superior Heavy Metal Removal. *Angew. Chem. Int. Ed.* **2025**, *64*, e202415051.
38. Song, J.; Hou, N.; Liu, X.; et al. Directional Formation of Reactive Oxygen Species via a Non-Redox Catalysis Strategy That Bypasses Electron Transfer Process. *Adv. Mater.* **2024**, *36*, 2405832.
39. Deng, S.; Liu, L.; Cagnetta, G.; et al. Mechanochemically Synthesized S-ZVI^{bm} Composites for the Activation of Persulfate in the pH-Independent Degradation of Atrazine: Effects of Sulfur Dose and Ball-Milling Conditions. *Chem. Eng. J.* **2021**, *423*, 129789.
40. Zitolo, A.; Goellner, V.; Armel, V.; et al. Identification of Catalytic Sites for Oxygen Reduction in Iron- and Nitrogen-Doped Graphene Materials. *Nat. Mater.* **2015**, *14*, 937–942.
41. Li, Q.; Luo, L.; Xu, C.; et al. Palladium Enhanced Iron Active Site—An Efficient Dual-Atom Catalyst for Oxygen Electroreduction. *Small* **2023**, *19*, 2303321.
42. Fan, P.; Wu, X.; Zeng, J.; et al. Resolve the Species-Specific Effects of Iron (Hydr)oxides on the Performance of Underlying Zerovalent Iron for Metalloid Removal: Identification of Their Key Properties. *J. Hazard. Mater.* **2024**, *477*, 135378.
43. Qin, H.; Sun, Y.; Yang, H.; et al. Unexpected Effect of Buffer Solution on Removal of Selenite and Selenate by Zerovalent Iron. *Chem. Eng. J.* **2018**, *334*, 296–304.
44. Liu, H.; Qian, T.; Zhao, D. Reductive Immobilization of Perrhenate in Soil and Groundwater Using Starch-Stabilized ZVI Nanoparticles. *Chin. Sci. Bull.* **2013**, *58*, 275–281.
45. Boglaienko, D.; Emerson, H.P.; Katsenovich, Y.P.; et al. Comparative Analysis of ZVI Materials for Reductive Separation of ^{99}Tc(VII) from Aqueous Waste Streams. *J. Hazard. Mater.* **2019**, *380*, 120836.
46. Shang, Y.; Ding, Y.; Zhang, P.; et al. Pyrrolic N or Pyridinic N: The Active Center of N-Doped Carbon for CO_2 Reduction. *Chin. J. Catal.* **2022**, *43*, 2405–2413.
47. Ha, Y.; Fei, B.; Yan, X.; et al. Atomically Dispersed Co-Pyridinic N-C for Superior Oxygen Reduction Reaction. *Adv. Energy Mater.* **2020**, *10*, 2002592.
48. Qin, M.; Chen, C.; Zhang, B.; et al. Ultrahigh Pyridinic/Pyrrolic N Enabling N/S Co-Doped Holey Graphene with Accelerated Kinetics for Alkali-Ion Batteries. *Adv. Mater.* **2024**, *36*, 2407570.
49. Yang, S.-M.; Guo, L.-L.; Nan, B.; et al. Tender Energy Spectroscopy Beamline at the Shanghai Synchrotron Radiation Facility. *Nucl. Sci. Tech.* **2025**, *37*, 11.